Materials Today Advances 29 (2026) 100678

Contents lists available at ScienceDirect

Materials Today Advances

journal homepage: www.journals.elsevier.com/materials-today-advances/

Volcanic deposits from mount Etna (Italy) as high-fidelity lunar simulants for In-Situ Resource Utilization (ISRU) applications

Giacomo Melchiori [a], Francesco Santoro De Vico [a,*], Alice Dottori [c], Riccardo Pozzobon [a,b,d], Luca Valentini [b], Patrizia Ferretti [e], Alessandro Bonetto [e], Michéle Lavagna [c], Sonia Calvari [f], Matteo Massironi [a,b]

[a] Center of Studies and Activities for Space "G. Colombo", University of Padova, Padova, Italy
[b] Department of Geosciences, University of Padova, Padova, Italy
[c] Department of Aerospace Science and Technologies, Politecnico di Milano, Milano, Italy
[d] Department of Physics and Astronomy, University of Padova, Padova, Italy
[e] Department of Environmental Sciences, Computer Science and Statistics, Ca' Foscari University of Venice, Venice, Italy
[f] Istituto Nazionale di Geofisica e Vulcanologia-Osservatorio Etneo (INGV-OE), Catania, Italy

A B S T R A C T

Terrestrial analogues of lunar regolith are crucial for developing In-Situ Resource Utilization (ISRU) technologies and testing mission hardware before lunar deployment. Mount Etna's (Southern Italy) diverse volcanic products, generated by complex slab-edge processes, offer exceptional compositional variability that encompasses both mare-like and highland-like lithologies, making it an ideal natural laboratory for planetary analogue studies. By investigating pyroclastic deposits and basaltic samples from the Cisternazza pit crater, and the Monte Nunziata and Tre Livelli lava tubes, we discovered that the sample from the Cisternazza pit crater exhibits remarkable chemical and mineralogical similarity to Apollo 14 highlands materials. The principal component analysis confirms its affinity with the lunar Fra Mauro formation samples, while X-ray diffraction reveals a plagioclase-pyroxene-olivine assemblage with 40 % amorphous phase mimicking lunar impact glass. VIS-NIR spectral signatures show characteristic 1-μm absorption features matching agglutinate-rich lunar regolith. Engineering geomechanical tests demonstrate that these materials achieve compressive strengths up to 16.40 MPa in earth environmental conditions when processed as alkali-activated materials, comparable to other lunar highlands simulants tested as reference materials for lunar construction. Our carbothermal reduction modeling indicates favorable oxygen and water extraction yields, validating Mount Etna volcanic deposits as high-fidelity simulants for advancing lunar ISRU technologies and mission preparation.

1. Introduction

Real lunar regolith samples are extremely limited and generally inaccessible, as only about 380 kg of soil and rock were returned to Earth during the Apollo missions [1]. Consequently, in the evolving landscape of space exploration there has been a growing need to develop substitute materials for use in scientific research for advancing our understanding of extraterrestrial environments and developing technologies for future missions [2]. These substitute materials could be used as essential tools for testing equipment, developing construction techniques, and validating In-Situ Resource Utilization (ISRU) processes before deployment in actual lunar missions [3,4].

Lunar simulants are derived from terrestrial materials and can either be used in their natural form (e.g., DNA-1A, LZS-1; [5,6]) or carefully produced by mixing various sources to replicate the chemical and mineralogical characteristics of specific lunar regions (e.g., NU-LHT series, OPRH series; [7]). Regardless of their origin, accurately reproducing the particle size distribution of lunar regolith is essential to effectively simulate its mechanical properties. However, both the development of artificial simulants or the fine-tuning of natural ones present significant challenges [8–10]. These include achieving accurate representation of lunar regolith properties, maintaining consistency across production batches, and ensuring availability for large-scale testing [11]. Despite decades of research [8–10], commercial availability remains limited. The NASA guidelines for lunar simulant characterization establish stringent criteria that materials must meet to be considered valid simulants [12]. These criteria encompass crucial parameters including chemistry, mineralogy, grain size distribution and grain shape analysis, determination of shear strength properties (cohesion and internal friction angle), minimum and maximum density measurements, and magnetic susceptibility analysis.

Most lunar simulants are produced in the United States [12] with only a few examples coming from Europe (e.g., DNA-1A, LZS-1). In this framework, the European volcanic provinces remain largely unexplored

* Corresponding author.
E-mail address: francesco.santoro@unipd.it (F. Santoro De Vico).

https://doi.org/10.1016/j.mtadv.2025.100678
Received 3 October 2025; Received in revised form 25 November 2025; Accepted 5 December 2025
Available online 12 December 2025

for this application [6,13]. Among them, Mount Etna (Fig. 1C) emerges as a unique geological setting. It is located on the eastern coast of Sicily (37°45′N, 14°59′E) and with its current elevation of approximately 3357 m a.s.l. Represents the largest active volcano in Europe. The volcano is at the intersection of the African and Eurasian plates, specifically where the Ionian oceanic lithosphere subducts beneath the Calabrian Arc [14,15]. This complex geodynamic setting, characterized by slab rollback and lateral tearing of the subducting plate [16], facilitates direct mantle upwelling that distinguishes Etna from typical arc volcanoes [17]. The volcanic products of Mount Etna are predominantly alkali basalts ($Na_2O + K_2O = 3.5–5.0$ wt%), with subordinate tholeiitic basalts ($Na_2O + K_2O < 3.5$ wt%) primarily found in the basal sequences [18]. The volcano has been continuously active for approximately 500,000 years, producing diverse volcanic deposits and morphological features including aa and pahoehoe lava flows, pyroclastic fall deposits, and extensive lava tube systems [19–21].

Sicilian law promotes the use of these volcanic materials, classifying volcanic ash fallout from recent explosive activity as a special municipal waste and allowing its reuse "to replace raw materials within production cycles, using processes or methods that do not harm the environment or endanger human health" [22]. While these ashes from nearby Etnean areas have been used for restoration purposes [23], those materials have never been utilized as lunar or asteroid regolith simulants.

In this study, three sites were selected based on their representativeness of different volcanic facies and their accessibility: (1) The **Tre Livelli Lava Tube System** (37° 42 ′31″N, 15° 03′ 45″E; 1625 m a.s.l.) (Fig. 1a, c) where samples TL-4 and TL-5 were collected from different levels of the lava tube to capture the variability within this volcanic structure that might also be manifested in lunar lava flows and tubes. (2) The **Monte Nunziata Lava Tube** (37° 44 ′52″N, 15° 02′ 11″E; 1790 m a.s.l.) (Fig. 1b, c) where sample MN-1 was collected from pyroclastic deposits situated behind the lining wall of the lava tube, representing material potentially similar to that found in lunar lava tube environments. (3) The **Cisternazza Pit Crater** (37° 45 ′18″N, 14° 59′ 42″E; 2600 m a.s.l.) (Fig. 1c, d). The crater floor and surrounding areas are mantled by recent pyroclastic fall deposits (grain size: 2–64 mm) from the paroxysmal events occurred during the last four decades [24], providing fresh, unweathered material ideal for simulating lunar regolith produced by volcanic activity and impact. Three samples were collected from this location: CL-2, CM-1 and CM-3 (Fig. 1c and Supplementary Table 1).

The chemical similarity of these materials to lunar regolith, combined with their accessibility, makes these three sites to collectively encompass a range of volcanic deposits and structures highly relevant for lunar simulant development. They provide promising analogues for various lunar geological features and material types, rather than just serving as construction materials. Their potential as simulants is further enhanced by the similarity in surface rugosity and shape [25,26] to lunar regolith particles [10], which is crucial for accurately replicating lunar soil properties [12]. In our approach to analyze these materials as potential lunar simulants, we adopted a modified version of the NASA workflow for simulant characterization (Fig. 2).

Our methodology was tailored to address specific research objectives, focusing primarily on identifying a high-fidelity chemical simulant suitable for ISRU tests. This focus led us to prioritize chemical composition over geotechnical properties, as even low-fidelity chemical simulants can be appropriate for geotechnical applications if they have the correct particle size distribution, a key factor influencing shear strength and internal friction angle [12].

This study offers a comprehensive assessment of Etnean volcanic materials as lunar regolith simulants, with particular emphasis on ISRU applications. Our multi-analytical approach combines screening techniques (principal component analysis of X-ray fluorescence data, X-ray diffraction) with in-depth characterization (scanning electron microscopy, hyperspectral imaging) and practical ISRU experiments (alkali-activated material synthesis, carbothermal reduction). Results demonstrate that selected Etnean deposits can closely mimic key properties of lunar regolith, particularly those of Apollo 14 highland materials [10]. We recognize that the concept of a "perfect" lunar simulant is challenging due to the fundamental differences between terrestrial and lunar

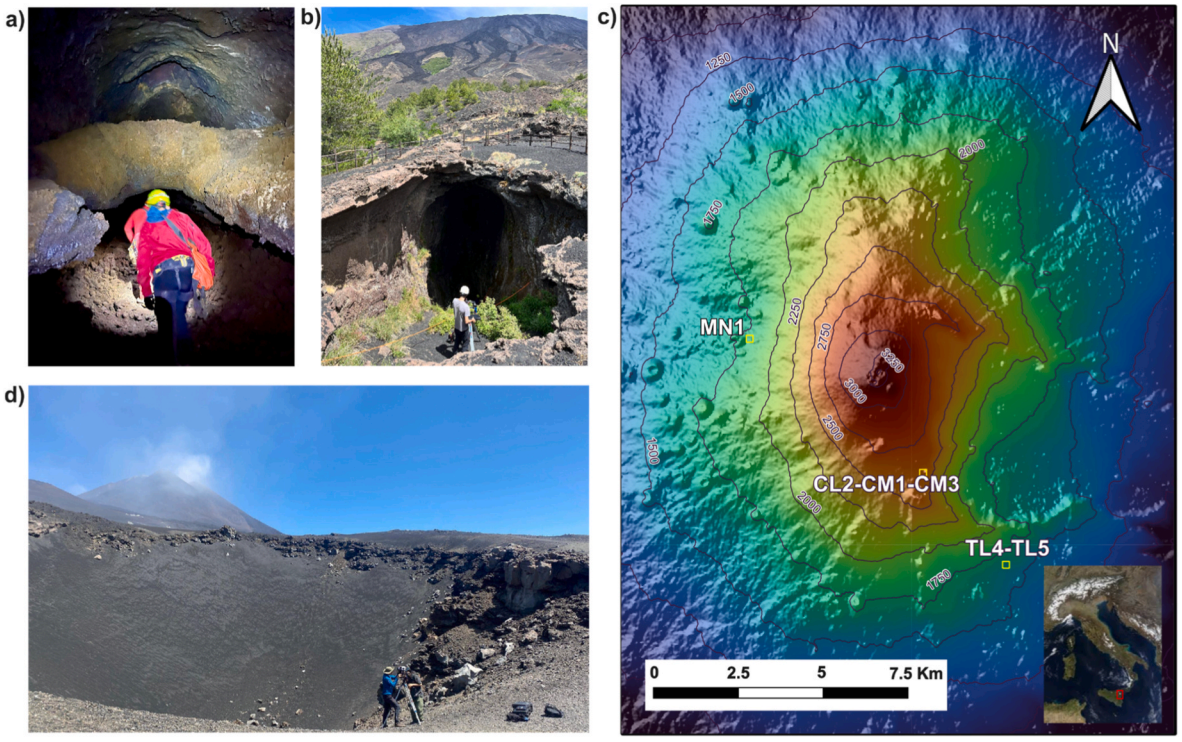

Fig. 1. Etna's sites in this study. a) Tre Livelli cave, 1792–93 eruption; **b)** Entrance of Monte Nunziata cave, 1843 eruption; **c)** Satellite image of sample location and isoline maps with the identification of the spot sites; **d)** Cisternazza pit crater, 1792–93 eruption.

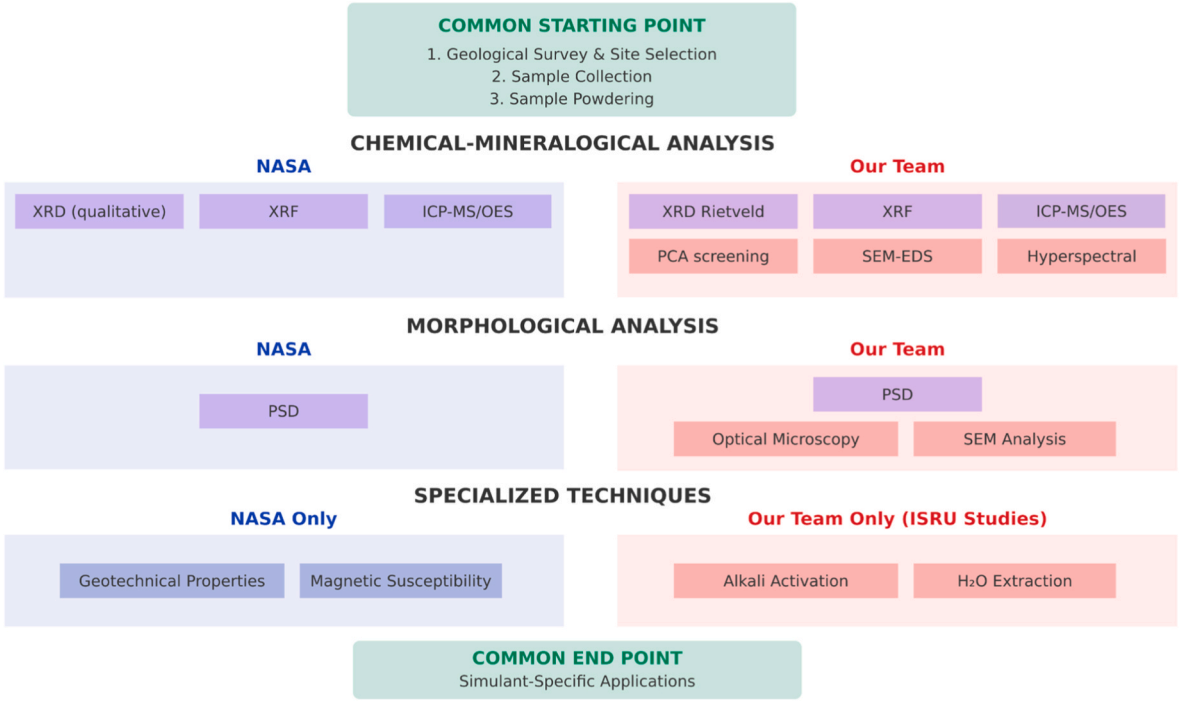

Fig. 2. Comparative analytical workflows for regolith simulant characterization. Both NASA (blue pathway) and our team (red pathway) begin with geological survey and sample preparation, then diverge into specialized analytical approaches before converging on simulant applications. Key methodological differences include our emphasis on quantitative mineralogy (Rietveld XRD), hyperspectral-PCA screening, and ISRU studies versus NASA's focus on geotechnical properties and magnetic susceptibility. All the acronyms are reported in Supplementary Table 7. (For interpretation of the references to color in this figure legend, the reader is referred to the Web version of this article.)

environments. Factors such as the absence of atmospheric weathering, different gravity conditions, and unique space weathering processes on the Moon create a regolith with properties that are difficult to fully replicate on Earth. Our findings, regarding the petrological and chemical aspects however, suggest that Etnean volcanic materials offer significant potential for advancing lunar ISRU technologies. The demonstrated capabilities in alkali-activated material synthesis and oxygen extraction highlight the potential of these materials for future lunar exploration efforts, providing a valuable and readily accessible resource for mission preparation and technology development.

2. Materials and methods

2.1. Sample preparation

To ensure material consistency and reproducibility of all the samples collected (Fig. S1), the **Retsch BB200** jaw crusher was run five times at a constant 650 rpm, progressively narrowing the jaw gap down to 1 mm to achieve the desired grain size reduction. Each crushing cycle lasted approximately 2 min, and the jaw gap was incrementally reduced between cycles to achieve a uniform particle size distribution. Subsequently the **Retsch RM0**, a small mill with agate grinding device, was used to reduce the grain size below 500 μm.

In order to ensure the homogenization and avoid problems in diffraction and spectroscopy analysis the materials were micronized for 5 min at 1500 rpm using deionized water with a **Retsch XRD-MILL MCCRONE.**

Subsequently, to estimate the mineralogical composition and the percentage of amorphous content an X-Ray Powder Diffraction analysis using an internal standard (10 % ZnO) was performed with a **Philips X'Pert Pro Diffractometer**, operating in para-focusing Bragg-Brentano geometry. For what concern the x-ray source a Co source (40 kV and 40 mA generator settings) was used and data were acquired through a continuous scan lasting 1 h (3–85° 2theta). For the qualitative and quantitative analysis, HighScore Plus [27] and Profex software [28] were used respectively.

The major- and trace-element composition of our samples was determined by wavelength-dispersive X-ray fluorescence (WDS-XRF) using a Panalytical Zetium sequential spectrometer operating under vacuum and controlled by SuperQ software. The instrument is equipped with a 2.4 kW Rh anode tube, five analyzing crystals (LiF220, LiF200, Ge, PE, PX1), three detectors (flow counter, scintillator, sealed Xe), two collimators (150 μm, 550 μm), and four primary-beam filters (Al 200 μm, Al 750 μm, Brass 100 μm, Brass 400 μm).

Approximately 1 g of powdered sample was ignited in a Nabertherm L15/11 furnace first at 860 °C for 20 min and then at 980 °C for 2 h to determine Loss On Ignition (LOI); the resulting calcined residue was then mixed with $Li_2B_4O_7$ flux (1:10 ratio) and fused at ≈ 1150 °C in a Claisse Eagon 2 to produce homogeneous glass beads for XRF. The furnace required about 1.5 h to reach 860 °C and an additional 30 min to reach 980 °C, corresponding to a controlled heating rate of approximately 9–10 °C/min in both stages.

Finally, the concentrations of major (Si, Ti, Al, Fe, Mn, Mg, Ca, Na, K, P) and trace (Sc, V, Cr, Co, Ni, Cu, Zn, Ga, Rb, Sr, Y, Zr, Nb, Ba, La, Ce, Nd, Pb, Th, U) elements were quantified by WDS-XRF, with routine analyses of natural geological standards [29] to monitor accuracy and precision.

2.2. Bulk screening methods

To efficiently identify samples whose bulk chemistry most closely resembles both established lunar regolith simulants and the average Apollo compositions—thereby avoiding time-consuming analyses on dissimilar materials—we applied a multivariate chemometric approach. Specifically, we performed principal component analysis (PCA) on the quantitative major element data obtained by XRF. This statistical screening rapidly highlighted those specimens clustering with reference compositions, which were then subjected to further study. To confirm

that chemical analogy translated into mineralogical similarity, we compared the XRD patterns of the PCA-selected samples against lunar reference phases. By integrating PCA-driven chemical selection with complementary XRD validation, we established a rigorous, two-tiered workflow for focusing detailed investigations on the most representative lunar analogues.

2.3. Inductively coupled plasma optical emission spectroscopy (ICP-OES)

Sample preparation for ICP-OES was conducted by weighing approximately 50 mg of material using an analytical balance (Practum, Sartorius, precision 0.01 mg). Samples were transferred into Teflon vessels for microwave-assisted acid mineralization (Ethos UP, Milestone). Each vessel was charged with a mixture of 6 mL aqua regia (HCl: HNO_3, 3:1 ratio) and 0.1 mL ultrapure HF. The sealed vessels were subjected to the heating program designated "Granite" (Supplementary Table 8), which comprised a 25-min heating ramp to 240 °C, a 15-min hold at maximum temperature, followed by a 20-min cooling phase to ambient temperature.

Following mineralization and cooling to room temperature, 0.5 mL of saturated H_3BO_3 solution was added to each digest and allowed to react for 2 h. The resulting solutions were quantitatively diluted to a final volume of 50 mL with ultrapure water. Aliquots of the stock solutions were further diluted at ratios of 1:10 for major element determination (Al, Ca, Fe, K, Mg, Na, Ti, Si) and 1:2 for trace element quantification (Ba, Cr, Cu, Mn, Ni, Pb, Sr, Zn).

Elemental analysis was performed using an inductively coupled plasma optical emission spectrometer (Perkin Elmer Optima 5300DV). Quantification was achieved through external calibration employing five-point calibration curves (concentration range 500–10,000 μg/L) for major elements and six-point calibration curves (concentration range 10–500 μg/L) for minor elements. Calibration parameters are presented in Supplementary Table 9.

The analytical wavelengths selected were: Ba λ = 233.527, Cr λ = 205.560, Cu λ = 324.752, Mn λ = 259.372, Ni λ = 231.604, Pb λ = 217.000, Sr λ = 421.552, Zn λ = 206.200 nm for minor constituents; Al λ = 308.215, Ca λ = 317.933, Fe λ = 238.204, K λ = 766.490, Mg λ = 258.213, Na λ = 589.592, Si λ = 252.851, Ti λ = 337.279 nm for major constituents.

The calibration curves exhibited an average correlation coefficient (R^2) of 0.999915, with values ranging from 0.999699 to 0.999993, demonstrating excellent linearity of the instrumental response across the investigated concentration range.

2.4. In-depth characterization of the selected sample

2.4.1. Particle size distribution reconstruction

The sample was sieved according to ASTM standards using sieve sizes 35, 60, 120, and 200 (500, 250, 125, and 75 μm respectively) to align the Particle Size Distribution (PSD) with Apollo samples [30]. This standardization is crucial for comparing our simulant with lunar regolith across various applications, including geotechnical properties and ISRU potential.

PSD analysis was performed using a Mastersizer 3000 laser diffraction instrument. As this instrument provides volume percentages rather than weight percentages (the standard for lunar data), we converted the results using an average density of 1.6 g/cm^3, based on lunar soil survey data [31]. This conversion ensures direct comparability with existing lunar regolith data.

To compare our PSD with lunar data, we normalized the curves by downsampling the higher-resolution data to match the resolution of the Apollo sample data. Similarity between PSDs was then assessed using three complementary metrics: (1) Jensen-Shannon divergence [32]: it measures the difference between two distributions by comparing each to their average. Low values indicate high similarity; (2) Pearson correlation [33]: it evaluates how closely the distributions rise and fall together. Values near +1 indicate strong linear correspondence; (3) Wasserstein distance [34]: it interprets distributions as mass distributions and calculates the average distance required to transform one into the other. Small distances indicate distributions concentrated in similar regions. These metrics provide a comprehensive evaluation of the similarity between our simulant's PSD and that of the lunar regolith, crucial for assessing its fidelity as a lunar analogue.

2.4.2. Thin section, optical and electron scanning microscopy

A thin section (30 μm) of the sample was prepared by embedding in epoxy and analyzed using optical microscopy. Elemental composition of major mineralogical phases and the amorphous component was determined using a SEM-CamScan MX3000 scanning electron microscope with energy-dispersive X-ray spectroscopy (EDS).

2.4.3. Hyperspectral acquisition

The sample, at different grain size: <75 μm, 125-75 μm, 250-125 μm, 500-250 μm, was acquired by two cameras: (1) Headwall Photonics Nano-Hyperspec (400–1000 nm; 270 spectral bands) and (2) Headwall Photonics Micro-Hyperspec (900–2500 nm; 166 spectral bands).

The data were processed in ENVI with its built-in Minimum Noise Fraction (MNF) transform to separate signal-rich components from noise-dominated ones, and Method 1 of Zhang et al. [35] was subsequently applied to remove the artificial peak at 2.1 μm that appears when a polytetrafluoroethylene (Spectralon-type) plaque is used as the NIR calibration target.

Continuum removal was applied by identifying two shoulder points (left and right) on either side of the absorption feature. A straight line (continuum) was calculated between these points for each spectrum using their corresponding reflectance values. The continuum-removed spectra were then obtained by dividing the original reflectance values within the selected wavelength range by this linear continuum (Fig. 6B), and the spectral parameters were then extracted using a custom Python script.

For a proper comparison with lunar samples we decided to take advantage of the spectrum acquired by RELAB of the lunar sample 14259; the 14259 specimen was analyzed in three configurations: the bulk soil as collected, the isolated agglutinate fraction, and the residue remaining after that agglutinates have been removed. Agglutinates are clusters of mineral and lithic fragments welded by impact-generated glass; they are a dominant constituent of many lunar soils, in some cases making up 60–70 % of the total mass. They originate when micrometeorite impacts locally melt small volumes of regolith and fuse the resulting glass with neighbouring particles. In fact, lunar regolith is continually modified by cosmic-ray bombardment, solar-wind sputtering, and pervasive micro-to nanometre-scale impacts that melt and vaporize material, subsequently redepositing it on neighbouring grains. These space-weathering processes generate nanophase metallic iron ($npFe^0$, also known as submicroscopic iron, SMFe) within the glass [36–38]. After all the correction process, the continuum was removed through a Python code and certain spectral parameters (centre, area, depth, full-width half maximum and asymmetry) were calculated around 1-μm both for our specimen and the lunar sample 14259.

2.4.4. Alkali-activated materials preparation

Four distinct alkali-activated mixtures were prepared using the Cisternazza CL2 powder as the precursor. The activating solutions comprised various combinations of sodium silicate (SS), sodium hydroxide (SH), and sodium aluminate (SA), as detailed in Table S7. Liquid-to-solid (L/S) ratios were 0.41 for Mix 1 (SS + SH), 0.30 for Mix 2 (SA + SH), 0.27 for Mix 3 (SA + SH), and 0.27 for Mix 4 (SA + SH with urea as an additive).

To assess the mechanical properties, prismatic specimens (40 × 40 × 160 mm) were cast in teflon molds after the use of a mechanical vibration. Samples underwent a 28-day curing period under controlled atmospheric conditions (25 °C, 65 % relative humidity), with demolding

after 3 days.

Uniaxial compressive strength tests were conducted on three specimens per mixture, following BS EN 12390–3:2002 [39]. Tests were performed using a universal testing machine (1500 kN capacity) with a constant loading rate of 2.6 kN/s until failure. The final compressive strength for each mixture was calculated as the mean of the three tested specimens.

2.4.5. *Demo plant for water extraction*

The solid carbothermal reduction process was used to extract oxygen from regolith simulants. This process involves heating oxides to high temperatures, below their melting point, in the presence of a methane and hydrogen flux. The oxygen is extracted in the form of carbon oxides, which are then converted to H_2O in a subsequent reaction step. The ISRU potential of the sample for water extraction was initially assessed using a carbothermal model based on its chemical composition determined by XRF analysis. This model utilized experimental results from previous campaigns with NU-LHT-2M simulant [40].

For the experimental procedure, 50 g of the sample were sieved to 250 μm and tested in a laboratory plant following a standard protocol [40,41]. The protocol entailed drying the sample in a static oven, followed by heating it to the reduction temperature at a rate 4 °C/min under an Argon flux of 0.1 SLM. Once the reduction temperature was achieved, the 8 h oxygen extraction phase commenced. To enhance CO extraction and extend the process duration, two phases were alternated during the extraction process: a mixing phase where a mixture of 85 %

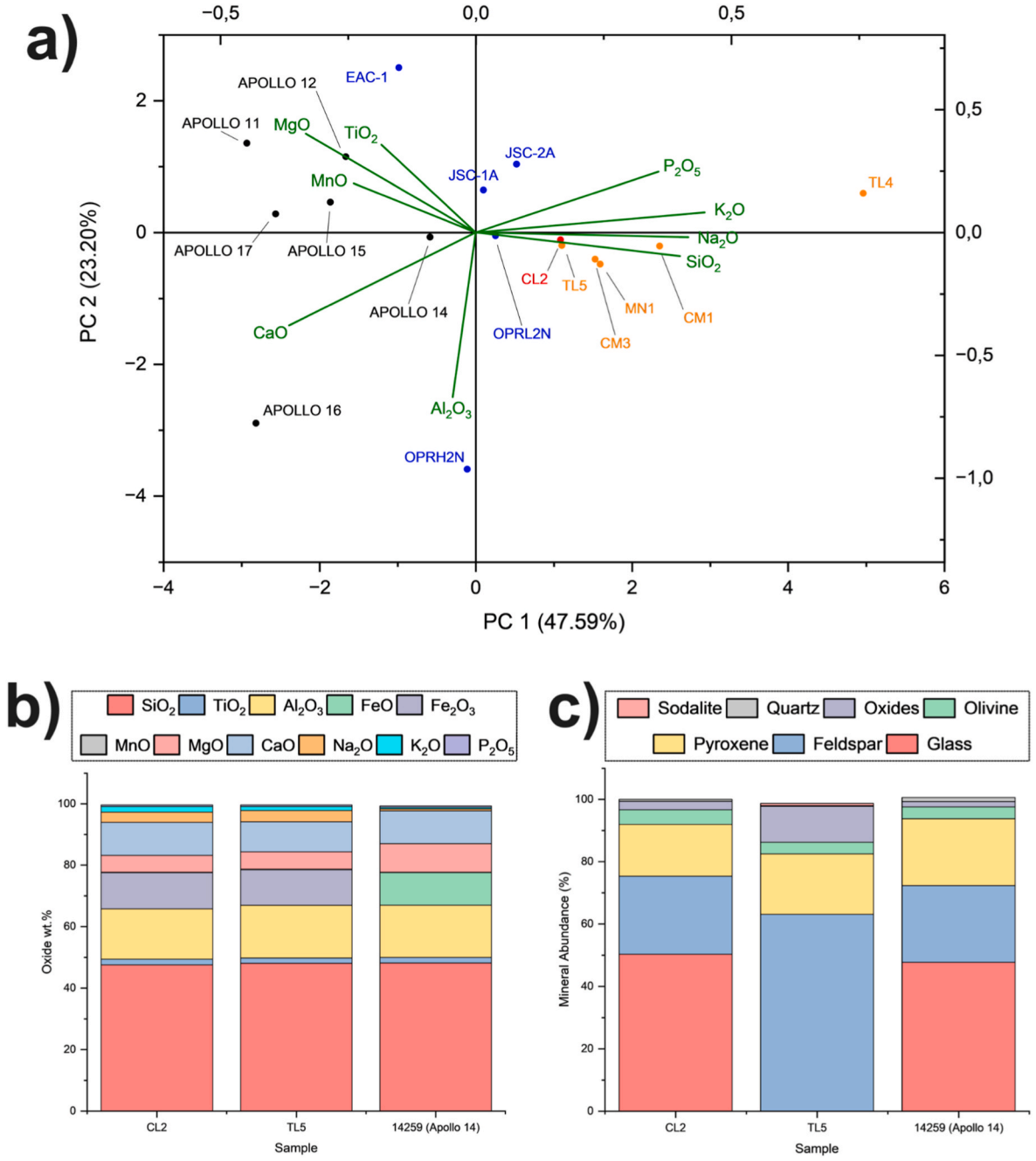

Fig. 3. Chemical screening using XRF and XRD. a) PCA comparing our samples (CL2, MN1, CM1, CM3, TL4, TL5) with the average composition of Apollo lunar samples and established lunar regolith simulants (EAC-1, JSC-1A, JSC-2A, OPRL2N, OPRH2N); **b)** Direct comparison of the chemical composition of CL2, TL5 and 14259 in terms of major elements. **c)** Direct comparison of the mineral assemblages in samples CL2, TL5, and 14259.

H_2/15 % CH_4 (vol%) was flowed through the reactor at a constant total flux of 0.5 L/min, and a washing phase where only H_2 was flowed through the reactor, allowing the deposited coke in the batch to react with the minerals. The main measure is the molar percentage of CO, CH_4, CO_2 and H_2 in the flow, retrieved from chromatograms acquired with a Shimadzu GCPro 2010 every 15–20 min using a TCD detector and a Resteck packed column; the column was operated with an initial temperature of 40 °C, followed by a 2-min holding time and a 40 °C/min ramp with additional holding steps at 100 °C, 140 °C and 150 °C. The TCD detector temperature was set to 180 °C.

Helium is exploited as a carrier gas. A calibration method has been defined to quantify the molar concentration of the gases by using eight calibration tanks with known concentrations of CO, CO_2, CH_4, H_2 and Ar provided by Sapio Group ®. A detailed description of the plant is available in the Supplementary materials and in Ref. [41].

3. Results

3.1. The bulk-screening method

Principal Component Analysis (PCA, Fig. 3A) on XRF analytical results was employed to screen six Etnean samples against Apollo mission compositions and established simulants. Two samples, CL2 (Cisternazza pyroclastics) and TL5 (Tre Livelli deposit), clustered closely with Apollo 14 highland materials (Fig. S1). Direct comparison with sample 14259 [31], a representative regolith sample collected 125 m west of the Apollo 14 Lunar Module [42], revealed remarkable similarities in major oxide compositions (Fig. 3B). The primary differences were the more elevated alkali contents of our samples (K_2O: 0.8 % vs 0.4 %; Na_2O: 3.2 % vs 0.6 %), consistent with Etna's alkaline volcanic character.

To verify that the chemical similarity translated to mineralogical correspondence, we performed quantitative XRD analysis on the PCA-selected samples (Fig. S2, Table 1, Table 2). Sample CL2 showed mineralogical proportions closely matching the 14259 reference (amorphous glass: 47.7 ± 2 %; feldspar: 24.6 ± 3 %; pyroxene: 21.5 ± 2 %; olivine: 3.8 ± 2 %). In contrast, TL5 exhibited excessive feldspar content (>55 %) and no glass (Fig. 3B), disqualifying it from further analysis (Fig. 3C).

Inductively Coupled Plasma Optical Emission Spectroscopy (ICP-OES) was performed to verify the XRF results. The comparison between the two techniques is shown in Fig. 5A-B. The plot presents the results of the XRF and ICP-OES analyses of CL2, along with the chemical composition of sample 14259 as reported by different authors [42–46] using various analytical techniques (Fig. 5A-B).

Following the screening phase, we aim to confirm and refine the compositional match between CL2 and lunar materials. Accordingly, we applied the Neal and Taylor classification [47], which links bulk TiO_2, Al_2O_3, and K_2O abundances to specific Apollo landing sites. As illustrated in Fig. 3A, CL2 plots in the low-Ti, high-Al field and occupies the high-K domain. This combined geochemical fingerprint matches that of samples returned by the Apollo 14 mission, supporting CL2 as a robust petrogenetic analogue for that site (Fig. 4A-B).

3.2. Particle size distribution

In this study, we reconstructed the particle size distribution (PSD) of CL2 by crushing the original sample and sieving it through four sieve sizes (500 μm, 250 μm, 125 μm, and 75 μm), with the aim of replicating the PSD of Apollo samples. While these four points provide precise control at those diameters, the intermediate portions of the distribution remain unconstrained and may deviate from natural lunar regolith. Each sieve fraction was analyzed individually, and for each, the 25th, 50th, and 75th percentiles were calculated and are reported in Table 3.

Despite this, the PSD of CL2 closely resembles the reference Apollo 14259 sample (Fig. 5C). Quartile grain sizes (Supplementary Table 2) show a slightly coarser fine fraction (Q25: 27.6 vs 22.1 μm) but a similar median (Q50: 51.8 vs 48.4 μm). Statistical comparisons after normalisation yielded a low Jensen-Shannon Divergence (0.0831), a strong Pearson correlation ($r = 0.8436$, $p = 0.0002896$), and a low Wasserstein Distance (1.367), all indicating a close match. A very low Jensen-Shannon divergence indicates near-identical overall shapes of the PSD curves. A Pearson correlation close to unity confirms strong linear agreement in fine-scale variations. Finally, a small Wasserstein distance shows that the majority of the probability mass is concentrated in the same phi-regions for both distributions.

3.3. Petrography and mineralogy

Petrographic analysis of sample CL2 (Fig. 6), conducted using optical microscopy and FE-SEM-EDX techniques, reveals a complex volcanic texture reminiscent of lunar pyroclastic deposits [51]. The sample exhibits a porphyritic texture within a hypocrystalline groundmass, indicating a complex cooling history similar to Apollo 14 basalts [52]. The amorphous component forms the skeleton of this raw material before the sieving process, with variable porosity: denser regions display circular voids ranging from 50 to 500 μm (Fig. 6B), while more compact areas feature macropores of approximately 400 μm in diameter (Fig. 6D, E, 6F).

The main phenocryst phases using EDX reveal forsteritic olivine ($Fo_{80\text{-}36}$), comparable to Apollo 15 green glass olivines [53], augitic clinopyroxene ($Wo_{46\text{-}78}En_{39\text{-}30}Fs_{13\text{-}59}$), consistent with lunar augites [54], and bytownitic plagioclase (An_{71}) (Supplementary Table 3). While plagioclase has slightly less calcium than typical lunar ones, it is still comparable to evolved portions of lunar basalts and terrestrial analogues used for simulant development [9] (Fig. 6D and G).

An important accessory phase of the CL2 sample is the iron-titanium spinel (titanomagnetite), significant for its potential in oxygen extraction for ISRU applications [55]. Its groundmass consists of microlites set in a glassy to cryptocrystalline matrix, resembling quench textures observed in lunar pyroclastic glasses [56,57].

In addition, having determined the elemental composition of the amorphous phase (glass) it is possible, following geochemical criteria [58], to determine which lunar glass type (pyroclastic glass, mare impact glass or highlands impact glass) our specimen most closely resembles.

To do this, two major elements ratio were calculated: (1) MgO/Al_2O_3, in particular the 1.25 ratio is a good discriminator between pyroclastic and impact glasses of the Moon; (2) CaO/Al_2O_3, the 0.75 ratio help us to distinguish between highland impact glass and mare impact glass of the Moon [59].

These analysis reveal for the CL2 sample MgO/Al_2O_3 and CaO/Al_2O_3 ratios of 0.29 (impact glass) and 0.55 (highland impact glass) respectively, placing CL2 within the highland impact-glass compositional field [53], as illustrated in Fig. 6H. This classification is supported by

Table 1
The oxide content results obtained from X-ray fluorescence analysis (XRF) on the selected samples after PCA. For comparison, the corresponding Apollo sample analysis is also included, sourced from Ref. [31].

	SiO_2	TiO_2	Al_2O_3	FeO	Fe_2O_3	MnO	MgO	CaO	Na_2O	K_2O	P_2O_5
CL2	47.5	1.9	16.4	/	11.7	0.2	5.5	10.8	3.3	1.8	0.5
TL5	48.1	1.7	17.1	/	11.6	0.2	5.7	9.8	3.6	1.4	0.5
14259 (Apollo 14)	48.1	1.8	17.0	10.1	/	0.1	9.3	10.7	0.7	0.5	0.5

Table 2
The mineral content results obtained from Rietveld refinement of X-ray powder diffraction (XRD) data for samples CL2 and TL5. For comparison, the corresponding analysis from the Apollo sample is also included [31].

	Glass	Feldspar	Pyroxene	Olivine	Oxides	Quartz	Sodalite
CL2	50.3	25.0	16.7	4.7	2.7	0.6	0
TL5	0	63.1	19.4	3.7	11.6	0.2	0.7
14259 (Apollo 14)	47.7	24.6	21.5	3.8	1.7	1.3	0

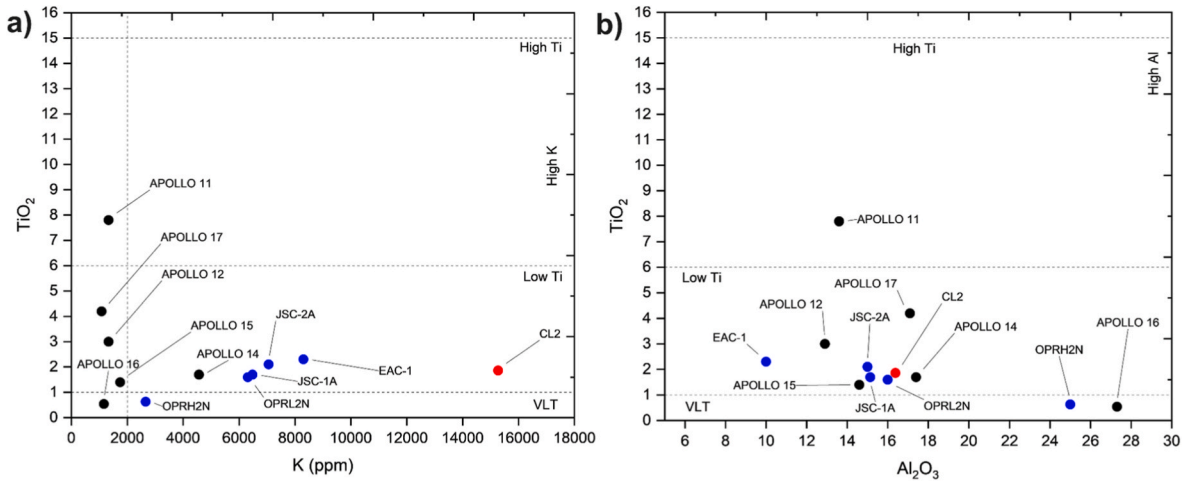

Fig. 4. Geochemical classification of lunar samples and simulants according to Neal & Taylor (1992). Commercial simulants are represented by blue dots, Apollo samples by black dots, and the analyzed sample by a red dot. **a)** Classification based on TiO_2 (wt%) versus K (ppm). Potassium concentrations were converted from K_2O wt% to elemental K in ppm using the stoichiometric conversion factor based on atomic masses ($K = 39.10$ g mol^{-1}; $K_2O = 94.20$ g mol^{-1}). **b)** Classification based on TiO_2 (wt%) versus Al_2O_3 (wt%). (For interpretation of the references to color in this figure legend, the reader is referred to the Web version of this article.)

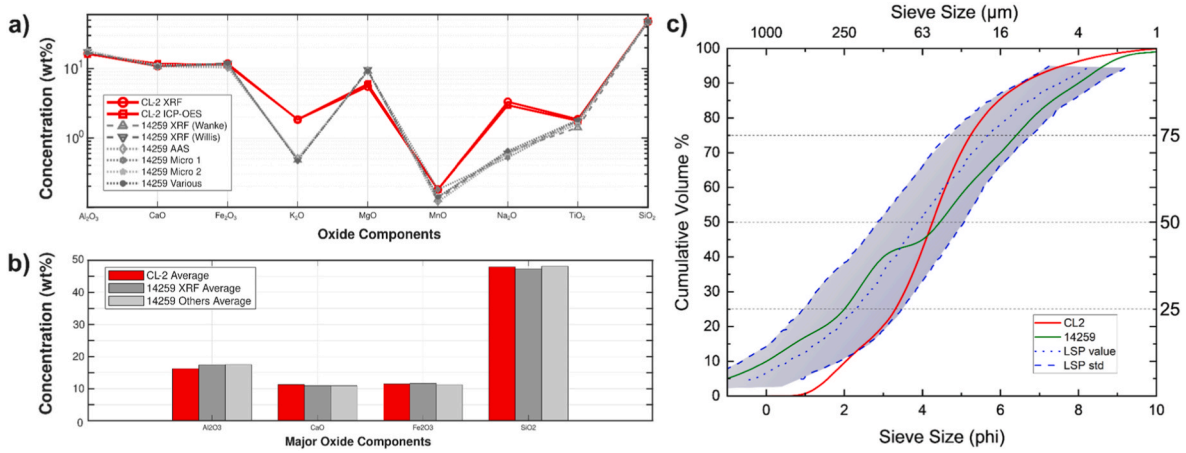

Fig. 5. Geochemical and grain size distribution comparison of CL2 and Apollo 14259 lunar samples using ICP-EOS, XRF and grain size distribution. a) Multi-element oxide composition analysis showing CL2 sample data (red symbols, solid lines) obtained via XRF (circles) and ICP-OES (squares) compared with Apollo 14259 literature data (gray symbols): XRF analyses (dashed lines with triangular markers from Refs. [45,46]), atomic absorption spectrometry (dotted line, diamonds from Ref. [42]), and microchemical analyses (dotted lines with various markers from [43,44,48]). Logarithmic scale emphasizes trace element variations alongside major components. **b)** Bar chart comparison of major oxide components (Al_2O_3, CaO, Fe_2O_3, SiO_2) showing averaged concentrations for CL2 sample, 14259 XRF techniques, and 14259 other analytical methods. Notable compositional differences include alkali enrichment (K_2O, Na_2O) in CL2 versus higher MgO content in 14259, reflecting distinct petrogenetic histories. Error bars represent analytical precision estimates based on inter-technique variability. **c)** Comparison between the cumulative distribution curve of CL2 (red line) and 14259 (green line), the grain size is expressed in phi units; the phi diameter is calculated as the negative logarithm to the base 2 of the particle diameter (in millimeters). The blue-dot middle curve shows the average lunar soil size particle distribution (LSP value), the left-hand and right-hand curves show ± one standard deviation (LSP std) [49]. (For interpretation of the references to color in this figure legend, the reader is referred to the Web version of this article.)

comparison with the reference lunar sample 14259, representative of Fra Mauro basaltic glass [60](Fig. 6H).

The presence of substantial glass content is particularly relevant for simulant applications, as glassy phases are abundant in lunar regolith due to impact melting and explosive volcanism forming pyroclasts [53, 61].

Space weathering processes, which create amorphous rims on lunar soil grains [62], further emphasize the importance of the amorphous glass component in CL2. In conclusion, CL2's petrographic and geochemical characteristics make it a promising simulant for lunar

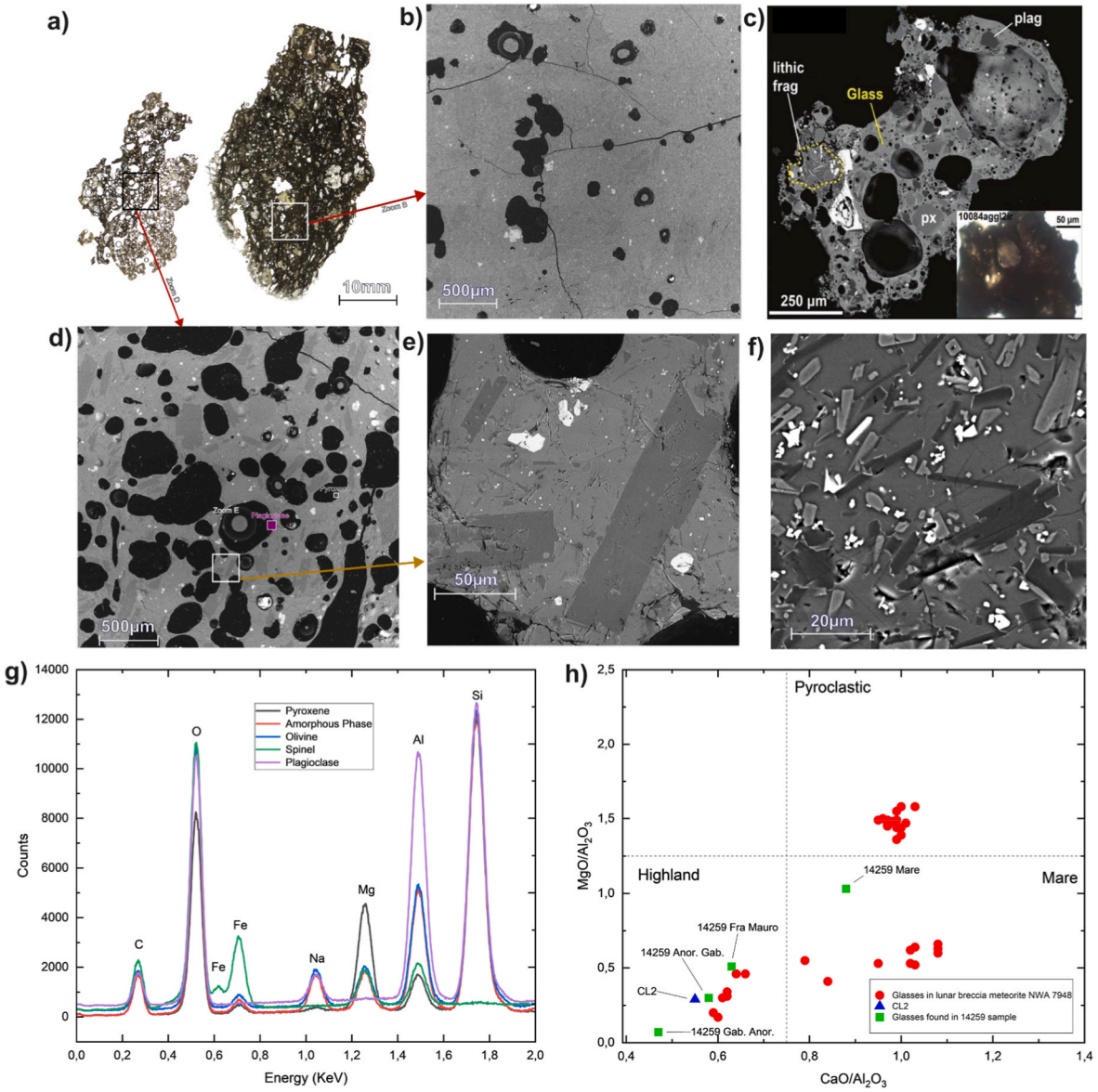

Fig. 6. Microscopy analysis and chemistry of CL2. a) Optical microscopy thin section overview of CL2 under parallel nicols; **b)** SEM detail of section A showing a low concentration of pores; **c)** backscattered electron image of an agglutinate from Apollo 11 [50]; **d)** SEM image of selected porous spots from image A, where different colors represent varying mineralogy of the sample, as highlighted in G with EDX; **e)** Detail of image D; **f)** Close-up of the amorphous matrix of CL2 with embedded crystals; **g)** EDX spectra of selected spots of the CL2 sample; **h)** MgO/Al_2O_3 and CaO/Al_2O_3 ratios of CL2 sample (blue triangle) compared to lunar samples (red dots and green squares). (For interpretation of the references to color in this figure legend, the reader is referred to the Web version of this article.)

Table 3
Each artificially produced sieve size was analyzed using a Mastersizer 3000 laser diffraction instrument and for each, the 25th, 50th, and 75th percentiles was calculated.

Original Sieve Size	D25 (µm)	D50 (µm)	D75 (µm)
500 µm<φ < 250 µm	~290	~382	~504
250 µm<φ < 125 µm	~129	~168	~217
125 µm<φ < 75 µm	~36	~64	~95
φ < 75 µm	~15	~30	~49

materials.

3.4. Hyperspectral acquisition

Hyperspectral analysis performed with Headwallphotonics devices in the 0.4–2.5 µm wavelengths range on four grain-size fractions revealed systematic variations in the 1-µm absorption feature for sample CL2. Fig. 7A and B also includes the spectra of three phases from soil sample 14259: (1) the bulk soil fraction, (2) magnetically separated agglutinates and (3) the low-agglutinate remnant obtained after agglutinate removal.

For CL2, the absorption center remained stable across all fractions, ranging from 1.0087 to 1.0280 µm, consistent with the pyroxene content. In Fig. 7A it clearly appears that the reflectance increases as particle size decreases [63]. On the other hand, the absorption depth (calculated as the difference between 1 and the minimum value of the continuum-removed spectrum) decreases with grain size from 0.218 (250–500 µm) to 0.143 (<75 µm) (Fig. 7B), following established physical principles for particulate materials.

As demonstrated by Cloutis et al. [64], a decrease in particle size in pyroxene initially leads to an increase in absorption band depth, up to a critical point (φ < 45 µm). Beyond this point, further reduction in grain size results in shallower absorption bands and reduced spectral contrast,

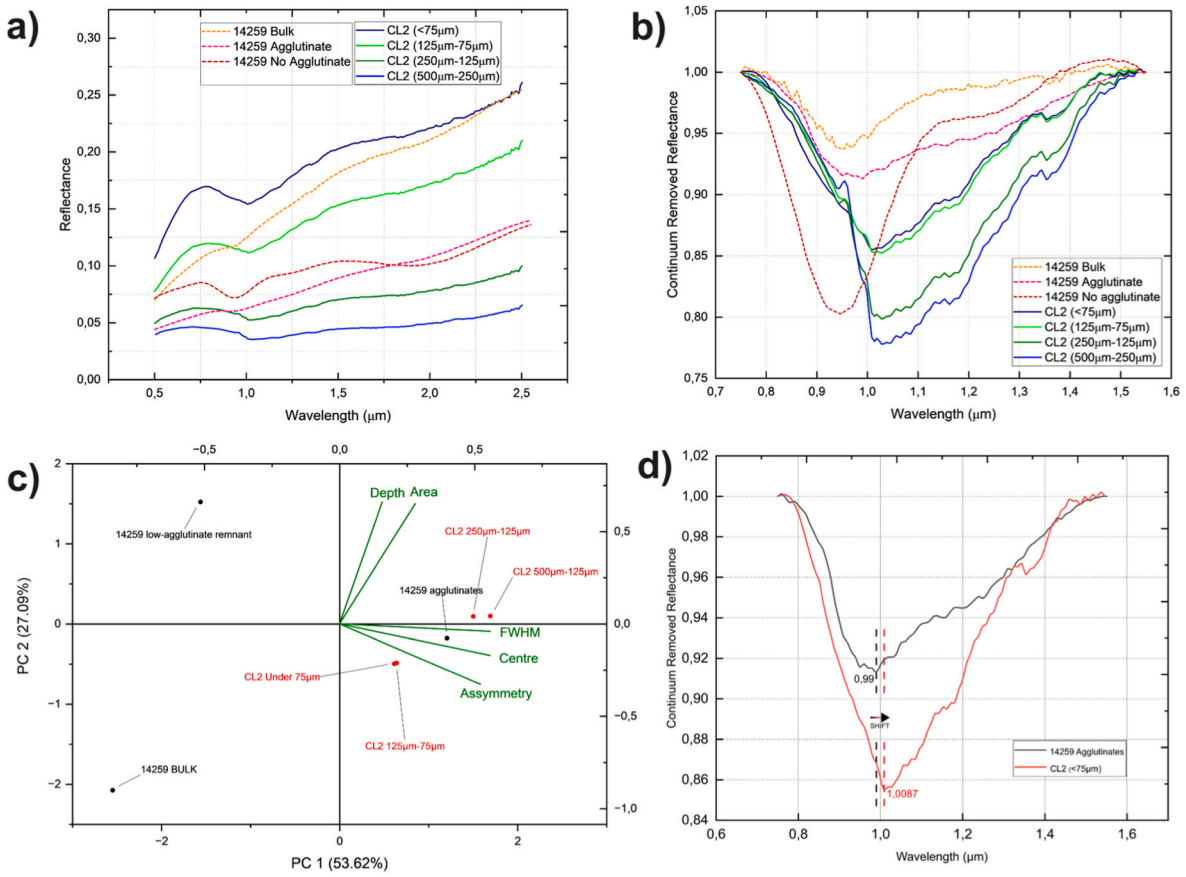

Fig. 7. Hyperspectral analysis on CL2 and Spectral comparison between CL2 and Apollo samples. a) Comparison between hyperspectral acquisitions at different grain sizes of CL2. **b)** Comparison between hyperspectral acquisitions at different grain sizes of CL2. **c)** PCA analysis of the spectral parameters from Apollo sample 14259 and CL2; **d)** Direct comparison of the CL2 and 14259 agglutinate spectra.

due to a shorter mean optical path length within the material. This effect is observed in the CL2 spectra shown in Fig. 7B for the $\varphi < 75$ µm and 75 µm $< \varphi <$ 125 µm fractions, which display reduced absorption depths. This likely indicates that these samples have reached or surpassed the turning point mentioned above. In support of this, the actual PSD measured in the lab for these fractions (Table 1) shows a clear shift toward finer grain sizes. For the Moon sample 14259, both the bulk soil and the low-agglutinate remnant exhibit the absorption center at 0.95 µm. In contrast, the agglutinate-rich fraction shows a red shifted absorption feature, centered at 0.99 µm, along with an increased asymmetry in the absorption band.

A principal component analysis (PCA) of the spectral parameters from Apollo sample 14259 and CL2 (Supplementary Tables 4–5) revealed a striking similarity between our sample and the agglutinate-rich fraction, particularly in the central wavelength, full width at half maximum (FWHM), and band asymmetry (Fig. 7C).

Additionally, we generated a direct comparison plot of the CL2 and 14259 agglutinate spectra to visually confirm the similarity suggested by their spectral parameters (Fig. 7D).

3.5. Building material potential

The compressive strength testing of alkali-activated materials prepared from the Cisternazza CL2 volcanic powder revealed significant performance variations across the four trial and error tested formulations using different activators like sodium aluminate (SA), sodium hydroxide (SH) and sodium silicate (SS) and one additive, urea in pellets (Supplementary Table 6). In Fig. 8A it is possible to note that, after 28 days of curing under atmospheric conditions (25 °C, 65 % Relative Humidity), Mix 3 (SA + SH, with a liquid to solid ratio = 0.27) achieved the highest average compressive strength of 16.40 ± 3.36 MPa. Mix 4, incorporating 3 % urea as an additive while maintaining the same liquid to solid ratio (L/S) and activator combination, demonstrated a compressive strength of 14.50 ± 1.00 MPa. Mix 1 (SS + SH, L/S = 0.41) exhibited intermediate performance with 12.89 ± 0.79 MPa, while Mix 2 (SA + SH, L/S = 0.30) recorded the lowest strength at 11.62 ± 1.59 MPa.

The coefficient of variation (CV) analysis revealed notable differences in mechanical property consistency across formulations. Mix 1 showed the highest reproducibility with CV = 6.1 %, followed by Mix 4 (CV = 6.9 %). Conversely, Mix 3 displayed substantial variability (CV = 20.5 %), despite achieving the highest absolute strength. The overall performance range of 11.62–16.40 MPa represents a 41.1 % variation between the lowest and highest performing mixtures (Fig. 8A).

3.6. Water extraction potential

The CL2 sample was also tested for water production with the solid-gas carbothermal process. The sample is reduced at a temperature of 1100 °C for 8 h, alternating phases in which a mixture of 85H_2/15CH_4 (vol%) is flown in the plant with phases during which only H_2(g) is flown in the reactor, for a total constant flow of 0.5 slm. Carbon oxides are obtained in this stage, which are then converted through methanation into water and methane. Fig. 8B shows the results of the CL2 test in terms of molar percentage of CO in the flow downstream of the carbothermal reactor.

The result is compared to the ones of certified lunar highlands simulants NU-LHT-2M [65] and LHS-1 [66], produced respectively by the U.S. Geological Survey and Space Resource Technologies. The CO trend is similar to that of the simulants, with an initial extraction peak

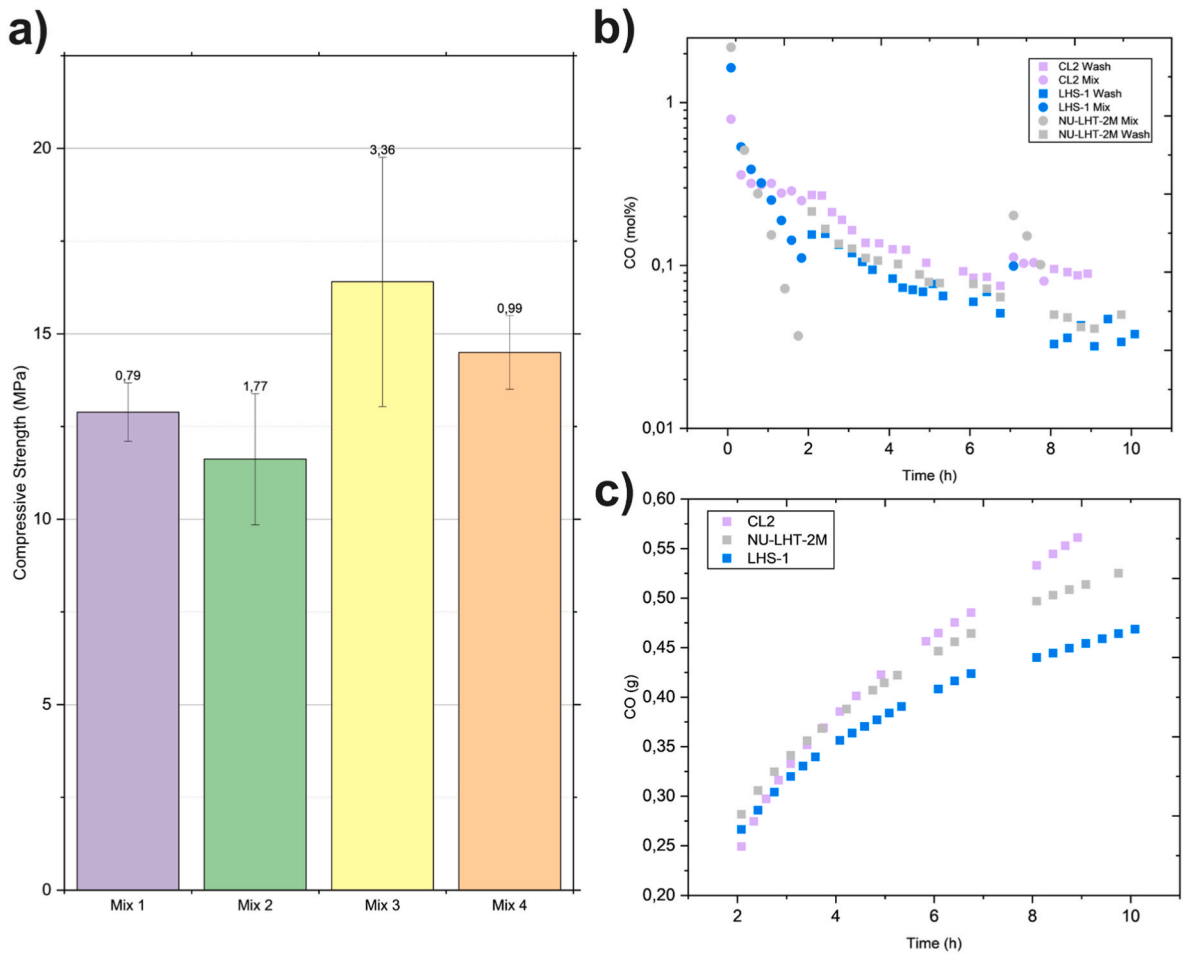

Fig. 8. ISRU potential in terms of building materials and water extraction. a) Compressive strength tests performed according to BS EN 12390–3:2002 standard [39] after 28 days curing at 25 °C and 65 % RH. **b)** Results in terms of molar percentage of CO (log10) in the flow downstream of the carbothermal reactor, retrieved from chromatograms. **c)** The integrated CO mass extracted during the carbothermal process, calculated from gas chromatograph data. For a mixing phase we use a mixture of 85 % H_2/15 % CH_4 (vol%) flowing through the reactor at a constant total flux of 0.5 L/min, and for the washing phase only H_2 flowing through the reactor.

followed by a stable production during the subsequent hours of the process. The initial CO peak is slightly lower compared to the artificial simulants, but in the first 2 h, the extraction trend is less concave. Similarly, there is almost no variation in CO mol% in the flow when the flux is switched from 85H_2/15CH_4 (squared markers in Figs. 8B) and 100H_2 (circular markers in Fig. 8B), meaning that the carbon deposited on the CL2 batch during the H_2/CH_4 phase reacts with the oxygen available in the sample during the H_2 phase.

4. Discussion

The differences between CL2 and the Apollo samples are principally Na_2O and K_2O (Figs. 3B and Fig. 5A–B). Although the compositional and isotopic similarities between Earth's primitive upper mantle (PUM) and the Moon suggest that the Moon originated from the proto-Earth, the Moon's inventory of volatile lithophile elements—such as Na, K, Rb, and Cs—is significantly lower than that of Earth's PUM, by factors of 4–5 [67].

The complex magmatic evolution and eruptive activity of Mount Etna play a role in these compositional differences. Magmatism in the area was triggered by diapiric upwelling of the mantle [68]; its evolution into three major phases [18] involved a dynamic interplay between mantle diapirism, a long-lived deep reservoir (20–30 km) of crystal mush and melt, and transient shallow magma chambers.

The deep reservoir, likely a remnant of the initial diapir, has supported continued magma differentiation, from tholeiitic to alkali basalts and trachybasalt, due to changing melting conditions and source compositions. Shallow magma storage has further driven the production of evolved lavas such as trachyandesites and trachytes. Persistent summit activity is fed by slow magma ascent and crystallization, while sudden pressure shifts and tectonic fracturing can open fissures and trigger explosive eruptions. These volcano-tectonic processes, along with episodic wall-rock assimilation, account for rapid variations in magma chemistry and eruptive behaviour observed over recent decades [18].

4.1. Petrography and mineralogy

From the mineralogical and petrographic point of view, the amorphous phase of CL2 and 14259 are similar in terms of abundance and composition, but their genetic process is fundamentally different (Fig. 6H). In the case of CL2, the glass phase is related to the rapid cooling that the lava underwent during an explosive eruption; whereas in the 14259 sample the glass phase is related to the continuous meteorite bombardment that the lunar regolith is subjected to. The maturity index (Is/FeO) is a way to measure how long lunar soil has been exposed at the surface. It compares how much weathering-produced nanophase iron is present (detected magnetically) to how much iron oxide was available. A higher value means the soil is more mature (older at the surface). In fact, Morris [69] reported the maturity index Is/FeO = 85

(mature). The high agglutinate count [70,71] and high carbon content [72] also indicate that this is representative of a very mature soil.

This difference in formation process could potentially influence some physical and chemical properties of the material. For instance, lunar impact glass might exhibit unique microstructures or inclusions not present in terrestrial volcanic glass, which could affect parameters such as the chemical reactivity or microscale mechanical properties. However, despite these genetic differences, our alkali activation and carbothermal reduction tests show comparable results between CL2 and certified lunar simulants. This suggests that for many ISRU applications, compositional similarity may be more relevant than the formation process.

4.2. Spectral properties

The spectral parameters of CL2 corroborate the SEM-EDS data: an absorption minimum at ~1.00–1.02 μm indicates Ca- and Fe-rich pyroxene accompanied by olivine [64,73], while a Fe-rich amorphous phase introduces a broad, shallow 1 μm band arising from disordered Fe^{2+} sites [74] (Fig. 7A-B). There are slight differences in spectral parameters moving to coarser grain sizes, even though the bulk composition remains essentially constant, about 50 % amorphous phase and 21 % pyroxene and olivine (XRD results) (Fig. 3C).

In the <75 μm sample, the fine grain size and physical distribution of volcanic glass, possibly coating or intimately mixed with mineral grains, result in a high specific surface area. This configuration enhances surface scattering, which reduces the effective path length for photons within mineral grains and increases the dominance of surface-related optical effects over volume absorption [75]. As a result, the glass can disproportionately absorb incident photons, leading to a suppression of the 1 μm absorption bands of pyroxene and olivine and a slight shift of their band minima toward shorter wavelengths [76]. Additionally, photons have a high probability of encountering a dark grain (e.g., dark volcanic glass), so even a small amount of dark material can significantly lower the overall reflectance of the mixture, far more than its weight fraction alone would suggest [63].

As grain size increases, the mass fraction of glass remains constant, but the surface-to-volume ratio decreases. Consequently, surface scattering becomes less dominant, allowing photons to penetrate deeper into the mineral grains and interact more with the bulk of uncoated augite and olivine crystals. This leads to a deepening of the 1 μm absorption band and a redward shift of its center toward the intrinsic positions of augite and olivine. The full width at half maximum (FWHM), however, remains nearly constant (Supplementary Table 4), as it is primarily controlled by mineral composition rather than particle size effects. The progressive increase in band asymmetry with grain size reflects the same transition: as glassy coatings lose optical dominance, the characteristic asymmetry of olivine and clinopyroxene becomes fully expressed [77].

A comparison between the spectral parameters of our specimen and those published for lunar sample 14259 reveals both analogies and distinctions. Concerning the spectral parameters that characterise the 1 μm absorption band (centre position, full width at half maximum, and asymmetry) our spectrum aligns most closely with the agglutinate fraction (Fig. 7B-D). Such agreement is expected because agglutinates, like our sample, consist of mineral fragments embedded in a glassy matrix. In fact, they have in common a single broad absorption band near 1-μm and a comparable asymmetry. But differences do emerge, reflecting contrasting formation histories that affect the optical behaviour of lunar agglutinates. For example, between the two samples (CL2 and 14259) there is a difference between the minimum at 1-μm of about 30 nm, because this kind of agglutinate is dominated by low-Ca orthopyroxene [31], whereas our sample is rich in high Ca augite; the increasing Ca and Fe move the centre to longer wavelengths in the Etna sample [78].

In addition, the lunar regolith is continually modified by cosmic-ray bombardment, solar-wind sputtering, and pervasive micro-to nanometre-scale impacts that melt and vaporize material, subsequently redepositing it on neighbouring grains. These space-weathering processes generate nanophase metallic iron ($npFe^0$, also known as submicroscopic iron, SMFe) within the glass [36–38]. This space-weathering makes the spectra darker and redder with respect to the undisturbed regolith [79]. Although it cannot be fully replicated on Earth, the spectral similarities between CL2 and lunar agglutinates, particularly in the 1 μm absorption feature, highlight the potential of Etnean materials as versatile lunar simulants for testing optical instruments and remote sensing technologies designed for lunar exploration.

4.3. Building material potential

The mechanical characterization of alkali-activated materials from Cisternazza CL2 volcanic powder reveals critical relationships between formulation parameters and structural performance relevant to lunar ISRU applications. The substantial strength increase from 11.62 to 16.40 MPa achieved by reducing the liquid/solid (L/S) ratio from 0.30 to 0.27 on the CL2 sample demonstrates the dominant role of the mixture density in controlling the mechanical properties (Fig. 8A). This 41.1 % improvement results from enhanced particle packing and reduced porosity, creating a denser microstructure with stronger interparticle bonding, consistent with established guidelines for alkali-activated materials formulation [80,81].

The performance of CL2 in alkali-activated formulations and carbothermal reduction experiments demonstrates its potential as a high-fidelity simulant for ISRU applications. However, it's crucial to consider that the behavior of these materials under lunar conditions (vacuum, reduced gravity) may differ from the Earth-based tests and future research should focus on developing methodologies to bridge this gap, e.g. by vacuum chamber experiments or computational modeling. Nevertheless, the abundant and easily accessible nature of Etnean volcanic materials offers the opportunity to refine and adapt our simulant as ISRU technologies evolve, potentially leading to a suite of simulants optimized for different stages of lunar resource utilization research.

The alkaline activator chemistry significantly influences both reaction kinetics and final properties. Despite its higher L/S ratio, the sodium silicate-activated Mix 1 achieved comparable strength to the sodium aluminate-activated Mix 2 (12.89 vs 11.62 MPa), indicating an enhanced reaction kinetics in the presence of sodium silicate, much likely due to higher pH. Given the chemical composition of the Etnean volcanic material ($CaO/Al_2O_3 = 0.66$, $(Na_2O + K_2O)/Al_2O_3 = 0.32$, $CaO/SiO_2 = 0.23$), it is expected that the alkali-activation process leads to the formation, as the main reaction products, of sodium aluminosilicate hydrate (N-A-S-H) with minor aluminium calcium silicate hydrate (C-A-S-H). According to established phase equilibria in alkali-activated systems, compositions with $CaO/SiO_2 < 0.4$ predominantly form N-A-S-H, while the available calcium (10.8 % CaO) acts primarily as a network modifier rather than forming discrete C-A-S-H phases [82]. This N-A-S-H-dominated gel structure provides enhanced chemical resistance and structural integrity through cross-linked aluminosilicate networks, with calcium incorporation contributing to improved mechanical properties without altering the fundamental gel chemistry [83]. The dual nature of the activator enhances both calcium dissolution from the volcanic glass matrix and promotes robust gel formation, compensating for the higher liquid content.

The incorporation of 3 % urea in Mix 4 exemplifies a strategic approach to balancing mechanical performance with processing reliability. While reducing average strength by 11.6 % compared to Mix 3, urea significantly improved the consistency of the results (reducing the coefficient of variation from 20.5 % to 6.9 %). This finding aligns with studies demonstrating urea's specific effectiveness as a water reducer for lunar alkali-activated materials in ISRU applications [84]. The improved consistency suggests homogeneous microstructure development, critical for quality control in automated construction systems.

Notably, the high variability in Mix 3 (CV = 20.5 %) despite its

superior strength highlights a fundamental challenge in low L/S ratio systems, where inefficient mixing and low workability may lead to microstructural heterogeneities. The achieved compressive strengths (11.62–16.40 MPa) indicate that the formulations developed using this lunar regolith simulant could potentially be reproduced on the Moon using actual lunar regolith, providing a basis for further research into lunar construction materials.

Considering the Moon's reduced gravity, the effective load-bearing capacity would be proportionally enhanced, making such materials suitable for habitat construction, landing pads, and radiation shielding structures as established in lunar construction research [85]. However, the full potential of volcanic alkali-activated materials for lunar applications would likely require adaptation of curing protocols to elevated temperature regimes consistent with lunar daytime conditions or controlled heating systems. The systematic tunability of properties through activator selection, L/S ratio optimization, and chemical additives provides essential flexibility for adapting materials to specific lunar construction scenarios, whether prioritizing maximum strength for critical structural elements or workability for robotic manufacturing systems.

4.4. Water extraction potential

The performance of the CL2 sample in water and oxygen extraction via the carbothermal reduction process is comparable to that of certified lunar highlands simulants, such as NU-LHT-2M [86]. Although the amount of water recovered during the condensation stage was lower than expected based on CO measurements, this discrepancy is attributed to limitations in the experimental plant system, specifically in the low efficiency of the condensation stage [41].

Fig. 8C reports the integrated CO mass extracted during the carbothermal process, based on gas chromatograph data. From these values, the corresponding water and oxygen masses were calculated by assuming complete conversion of CO to H_2O during methanation. The mass trends were consistent across all tested samples, reflecting their similar bulk composition. CL2 contained a higher fraction of ferrous oxides compared to NU-LHT-2M and LHS-1, which increased its reactivity with hydrogen and supported faster reduction during the hydrogen-only process steps.

This higher reactivity makes CL2 comparable not only to highland simulants but also to maria-type simulants such as LMS-1. The reproducibility of the results, together with the enhanced reduction behavior, indicates that CL2 is a reliable material for oxygen extraction. These findings confirm its potential for use in ISRU processes aimed at extracting the oxygen from the regolith and supporting long-term lunar exploration.

4.5. Consideration of lunar environmental conditions

All experiments were conducted under terrestrial conditions (25 °C, 1 atm), yet the lunar environment presents distinct challenges, specifically vacuum (10^{-12} Pa), reduced gravity (1/6 g), and extreme thermal cycling. The thermal range varies significantly with lunar location. Equatorial regions, such as Mare Tranquillitatis, exhibit the largest diurnal temperature excursions, from approximately −170 °C to +120 °C. Mid-latitude areas show a somewhat narrower range, typically from about −190 °C to +60 °C, while polar regions experience persistently cold conditions with temperatures generally spanning −223 °C to −73 °C, depending on illumination geometry. (see Supplementary Figs. 3–4). Recent studies demonstrate that geopolymers retain >70 % compressive strength after thermal cycling between −40 °C and +120 °C [87,88]; this range does not correspond to any lunar thermal environment and was selected mainly due to instrumental limitations in the experiments.

However, the combined effects of thermal cycling and vacuum exposure present compounded risks. Water evaporation during alkali activation under vacuum (2×10^{-6} atm) can increase porosity and reduce mechanical properties by 8–40 % [89]. When both degradation mechanisms are considered, a ~30 % reduction from thermal cycling together with up to a ~40 % reduction from vacuum-induced effects, the cumulative strength loss could approach 60–70 %, bringing the material dangerously close to structural limits. While reduced lunar gravity means structures bear only one-sixth of the load they would experience on Earth, this gravitational advantage may be insufficient to compensate for severe combined degradation. For example, a 16 MPa material reduced to 10 MPa on the Moon would still perform equivalently to a 60 MPa material on Earth when accounting for the reduced gravitational stress. This suggests that site selection should prioritize thermally stable locations, such as polar regions or permanently shadowed craters, where temperature fluctuations are minimized. Alternatively, engineering solutions such as thermal insulation or protective regolith covering could mitigate extreme temperature exposure for structures in equatorial regions.

Carbothermal reduction, however, faces more complex challenges. Ultra-high vacuum alters reaction thermodynamics and kinetics. Shaw et al. [90] demonstrated that while Fe and Si reduction from mare regolith remains thermodynamically favorable at 200 °C and 1050 °C, respectively, under 10^{-12} atm, the reaction rates decrease significantly. Furthermore, maintaining thermal control without convective heat transfer and ensuring gas confinement in a vacuum present substantial engineering hurdles for scaling this process [91]. Another factor is that, depending on the mass of solid feedstock to be reduced, the gases might interact with a fluidised bed instead of a fixed one. While this may be detrimental to the heating phase, it can promote gas-solid interactions. Future work should prioritize vacuum chamber testing of both alkali activation and carbothermal processes using CL2 to quantify these effects and develop appropriate mitigation strategies for lunar deployment.

5. Conclusions

This study presents a comprehensive evaluation of volcanic materials from Mount Etna as potential lunar regolith simulants, with particular emphasis on their applicability to In-Situ Resource Utilization (ISRU) processes. Our multi-analytical approach, combining geological and petrological characterization, spectral analysis, and geomechanical testing, provides robust evidence for the suitability of specific Etnean materials as lunar analogues.

Principal component analysis of bulk chemistry and mineralogical data identified the CL2 sample from the Cisternazza pit crater as the closest terrestrial analogue to Apollo 14 Fra Mauro formation materials. X-ray diffraction revealed a mineralogical assemblage comparable to magnesian suite lithologies (e.g., gabbros and norites), while hyperspectral analysis confirmed a 1-μm absorption feature consistent with agglutinate-rich highland soils. The substantial amorphous fraction in CL2 shares compositional traits with lunar impact-derived glasses, although it is of volcanic origin.

Engineering tests demonstrate that alkali-activated products derived from CL2 develop promising compressive strength values, supporting its potential use in lunar construction simulants. Moreover, preliminary carbothermal reduction modeling indicates favorable conditions for water and oxygen extraction, underscoring its relevance for ISRU applications.

It must be emphasized, however, that these results were obtained under terrestrial conditions. When considering actual lunar environmental parameters, such as vacuum, reduced gravity, and extreme temperature fluctuations, additional challenges may arise that could affect both the mechanical performance and ISRU efficiency of CL2. Future work should therefore aim to experimentally reproduce such conditions to validate the material's behavior under true in-situ scenarios.

In summary, the CL2 deposit from Mount Etna's Cisternazza pit

crater constitutes a high-fidelity simulant for Apollo 14 Fra Mauro formation materials, exhibiting strong potential for ISRU-related applications in lunar construction and resource extraction.

CRediT authorship contribution statement

Giacomo Melchiori: Writing – review & editing, Writing – original draft, Visualization, Validation, Software, Resources, Project administration, Methodology, Investigation, Formal analysis, Data curation, Conceptualization. **Francesco Santoro De Vico:** Writing – review & editing, Writing – original draft, Visualization, Validation, Supervision, Software, Resources, Project administration, Methodology, Investigation, Formal analysis, Data curation, Conceptualization. **Alice Dottori:** Writing – review & editing, Methodology, Data curation. **Riccardo Pozzobon:** Writing – review & editing, Visualization, Supervision, Software, Project administration, Methodology, Investigation, Funding acquisition, Data curation, Conceptualization. **Luca Valentini:** Writing – review & editing, Visualization, Methodology. **Patrizia Ferretti:** Writing – review & editing, Supervision, Methodology. **Alessandro Bonetto:** Writing – review & editing, Methodology, Data curation. **Michéle Lavagna:** Writing – review & editing, Supervision. **Sonia Calvari:** Writing – review & editing, Visualization, Supervision, Methodology. **Matteo Massironi:** Writing – review & editing, Visualization, Supervision, Project administration, Methodology, Investigation, Funding acquisition, Conceptualization.

Declaration of competing interest

The authors declare that they have no known competing financial interests or personal relationships that could have appeared to influence the work reported in this paper.

Acknowledgments

We want to dedicate this article to our colleague and friend Riccardo Pozzobon. This work is also dedicated to the memory of Salvatore De Vico, grandfather of Francesco, who passed away during the preparation of this manuscript. His values will forever inspire him and his family. This study was carried out within the Space It Up project funded by the Italian Space Agency, ASI, and the Ministry of University and Research, MUR, under contract n. 2024-5-E.0 - CUP n. I53D24000060005. The carbothermal investigation was carried on within the ORACLE project, funded by ASI under the contract 2023-11-HH.0.

Appendix A. Supplementary data

Supplementary data to this article can be found online at https://doi.org/10.1016/j.mtadv.2025.100678.

Data availability

Correspondence and material requests should be addressed to Giacomo Melchiori at giacomo.melchiori@phd.unipd.it or to Francesco Santoro De Vico at francesco.santoro@unipd.it. All the available raw data are provided in a github branch at this link: https://github.com/PacoSanto/Data_Availability_papers/tree/aea13b27a5efc8c6a44728ff840a5a5ebc060690/Communications%20Earth%20%26%20Environment_Volcanic%20deposits%20from%20Mount%20Etna%20as%20high-fidelity%20lunar%20simulants%20for%20ISRU%20applications.

References

[1] S. Lim, V.L. Prabhu, M. Anand, L.A. Taylor, Extra-terrestrial construction processes–Advancements, opportunities and challenges, Adv. Space Res. 60 (7) (2017) 1413–1429.
[2] L.A. Taylor, C.M. Pieters, D. Britt, Evaluations of lunar regolith simulants, Planet. Space Sci. 126 (2016) 1–7.
[3] M. Anand, et al., A brief review of chemical and mineralogical resources on the moon and likely initial in situ resource utilization (ISRU) applications, Planet. Space Sci. 74 (2012) 42–48.
[4] F. Foucher, et al., Definition and use of functional analogues in planetary exploration, Planet. Space Sci. 197 (2021) 105162.
[5] V. Marzulli, F. Cafaro, Geotechnical properties of uncompacted DNA-1A lunar simulant, J. Aero. Eng. 32 (2019) 04018153.
[6] F. Alberquilla, J. Martínez-Frías, V. García-Baonza, R. Lunar, LZS-1, lanzarote (Canary Island, Spain) lunar (Apollo 14) basaltic soil simulant, Sci. Rep. 12 (2022) 16470.
[7] Y.C. Toklu, P. Akpinar, Lunar soils, simulants and lunar construction materials: an overview, Adv. Space Res. 70 (3) (2022) 762–779.
[8] P.W. Weiblen, K. Gordon, Characteristics of a simulant for lunar surface materials, in: Second Conference on Lunar Bases and Space Activities of the 21st Century, vol. 652, 1988, p. 254.
[9] D.S. McKay, J.L. Carter, W.W. Boles, C.C. Allen, J.H. Allton, JSC-1: a new lunar soil simulant, Engineering, Construction, and Operations in Space IV 2 (1994) 857–866.
[10] E. Hill, M.J. Mellin, B. Deane, Y. Liu, L.A. Taylor, Apollo sample 70051 and high- and low-Ti lunar soil simulants MLS-1A and JSC-1A: implications for future lunar exploration, J. Geophys. Res. Planets 112 (2007) E02006.
[11] J.R. Gaier, The need for high fidelity lunar regolith simulants, NASA Technical Memorandum No. E-16528 (2008).
[12] A. Slabic, et al., Lunar Regolith Simulant User's Guide: Revision A. NASA Technical Memorandum No. NASA/TM-20240011783, 2024.
[13] E. Mateo, J. Martínez-Frías, J. Vegas (Eds.), Lanzarote and Chinijo Islands Geopark: from Earth to Space, Springer International Publishing, 2019.
[14] Z. Gvirtzman, A. Nur, The formation of Mount Etna as the consequence of slab rollback, Nature 401 (1999) 782–785.
[15] C. Doglioni, F. Innocenti, G. Mariotti, Why Mt etna? Terra Nova 13 (2001) 25–31.
[16] G. Barreca, S. Branca, R.A. Corsaro, L. Scarfì, F. Cannavò, M. Aloisi, et al., Slab detachment, mantle flow, and crustal collision in eastern sicily (southern Italy): implications on Mount Etna volcanism, Tectonics 39 (2020), https://doi.org/10.1029/2020TC006188 e2020TC006188.
[17] W.P. Schellart, Mount Etna–Iblean volcanism caused by rollback-induced upper mantle upwelling around the Ionian slab edge: an alternative to the plume model, Geology 38 (2010) 691–694.
[18] J.C. Tanguy, M. Condomines, G. Kieffer, Evolution of the Mount Etna magma: constraints on the present feeding system and eruptive mechanism, J. Volcanol. Geoth. Res. 75 (3–4) (1997) 221–250.
[19] S. Branca, M. Coltelli, G. Groppelli, Geological evolution of a complex basaltic stratovolcano: mount Etna, Italy, Ital. J. Geosci. 130 (2011) 306–317.
[20] S. Branca, et al., Geological evolution of Mount Etna volcano (Italy) from earliest products until the first central volcanism (between 500 and 100 ka ago) inferred from geochronological and stratigraphic data, Int. J. Earth Sci. 97 (1) (2008) 135–152.
[21] S. Calvari, G. Giudice, R. Maugeri, D. Messina, D. Morgavi, L. Miraglia, A. La Spina, L. Spampinato, Complex lava tube networks developed within the 1792–93 lava flow field on Mount Etna (Italy): insights for hazard assessment, Front. Earth Sci. 12 (2024) 1448187, https://doi.org/10.3389/feart.2024.1448187.
[22] Legge n. 108, Conversione in legge, con modificazioni, del decreto-legge 31 maggio 2021, n. 77, Gazzetta Ufficiale della Repubblica Italiana, Serie Generale n.181 del 30-07-2021 (2021).
[23] G. Barone, C. Finocchiaro, I. Lancellotti, C. Leonelli, P. Mazzoleni, C. Sgarlata, A. Stroscio, Potentiality of the use of pyroclastic volcanic residues in the production of alkali activated material, Waste Biomass Valoriz. 12 (2) (2021) 1075–1094.
[24] S. Calvari, G. Nunnari, Etna output rate during the last decade (2011–2022): insights for hazard assessment, Remote Sens. 14 (2022) 6183, https://doi.org/10.3390/rs14236183.
[25] D. Andronico, S. Scollo, A. Cristaldi, F. Ferrari, Monitoring ash emission episodes at mt. Etna: the 16 November 2006 case study, J. Volcanol. Geoth. Res. 180 (2009) 123–134.
[26] D. Andronico, P. Del Carlo, PM10 measurements in urban settlements after lava fountain episodes at mt. Etna, Italy: pilot test to assess volcanic ash hazard to human health, Nat. Hazards Earth Syst. Sci. 16 (2016) 29–40.
[27] T. Degen, M. Sadki, E. Bron, U. König, G. Nénert, Journal of powder diffraction, Powder Diffr. 29 (S2) (2014) S13–S18, https://doi.org/10.1017/S0885715614000840.
[28] N. Döbelin, R. Kleeberg, Profex: a graphical user interface for the Rietveld refinement program BGMN, J. Appl. Crystallogr. 48 (2015) 1573–1580.
[29] K. Govindaraju, F.R.A. Vandoeuvre-Lès-Nancy, Geostand. Newsl. 19 (Special Issue, July) (1994).
[30] J.C. Graf, *Lunar Soils Grain Size Catalog*. NASA Ref, Publ. No. 1265 (NASA, 1993.
[31] Charles Meyer, Lunar Sample Compendium, 2005.
[32] M.L. Menéndez, J.A. Pardo, L. Pardo, M.D.C. Pardo, The Jensen-Shannon divergence, J. Franklin Inst. 334 (1997) 307–318.
[33] K. Pearson, Note on regression and inheritance in the case of two parents, Proc. Roy. Soc. Lond. 58 (1895) 240–242.
[34] Y. Rubner, C. Tomasi, L.J. Guibas, The Earth Mover's distance as a metric for image retrieval, Int. J. Comput. Vis. 40 (2000) 99–121.
[35] H. Zhang, et al., Effects of spectralon absorption on reflectance spectra of typical planetary surface analog materials, Opt. Express 22 (2014) 21280–21291.
[36] S. Noble, The lunar regolith. *Lunar Regolith Simulant Workshop* MSFC-2221, 2009.

[37] C. James, et al., Size distribution of Fe^0 globules in lunar agglutinitic glass, in: 33rd Lunar Planet. Sci. Conf. Abstract #1827, 2002.
[38] L.P. Keller, S.J. Clemett, Formation of nanophase iron in the lunar regolith, in: 32nd Lunar Planet. Sci. Conf. Abstract #2097, 2001.
[39] British Standards Institution. Testing hardened concrete, Compressive strength of test specimens, BS EN 12390–3 (2009).
[40] A. Dottori, I. Troisi, M.R. Lavagna, Demonstration of the low-temperature carbothermal process for producing oxygen from lunar regolith: terrestrial test campaign, Planet. Space Sci. (2025) 106154.
[41] J. Prinetto, A. Colagrossi, A. Dottori, I. Troisi, M.R. Lavagna, Terrestrial demonstrator for a low-temperature carbothermal reduction process on lunar regolith simulant: design and AIV activities, Planet. Space Sci. 225 (2023) 105618.
[42] C.C. Schnetzler, D.F. Nava, Chemical composition of apollo 14 soils 14163 and 14259, Earth Planet Sci. Lett. 11 (1971) 345–350.
[43] LSPET, Preliminary examination of lunar samples from apollo 14, Science 173 (1971) 681–693.
[44] H.J. Rose Jr., F. Cuttitta, C.S. Annell, M.K. Carron, R.P. Christian, E.J. Dwornik, L. P. Greenland, D.T. Ligon Jr., Compositional data for twenty-one Fra Mauro lunar materials, in: Proceedings of the Third Lunar Science Conference, Lunar and Planetary Science Conference, 1972, pp. 1215–1229.
[45] H. Wänke, H. Baddenhausen, A. Balacescu, F. Teschke, et al., Multielement analyses of lunar samples and some implications of the results, in: Proceedings of the 3rd Lunar Science Conference, 1972 (Abstract 1251).
[46] J.P. Willis, A.J. Erlank, J.J. Gurney, R.H. Theil, L.H. Ahrens, Major, minor, and trace element data for some apollo 11, 12, 14 and 15 samples, in: Proceedings of the Lunar and Planetary Science Conference, vol. 3, Lunar and Planetary Science Conference, 1972.
[47] C.R. Neal, L.A. Taylor, Petrogenesis of mare basalts: a record of lunar volcanism, Geochem. Cosmochim. Acta 56 (1992) 2177–2211.
[48] A. Strasheim, P.F.S. Jackson, J.H.J. Coetzee, F.W.E. Strelow, F.T. Wybenga, A. J. Gricius, R.H. Scott, Analysis of lunar s, in: Amples 14163, 14259, and 14321 with Isotopic Data for 7Li/6Li. in Proceedings of the Lunar Science Conference, vol. 3, 1972, p. 1337, vol. 3, p. 1337.
[49] D. Carrier, The four things you need to know about the geotechnical properties of lunar soil, Lunar Geotechnical Institute (2005) 2–9.
[50] F.M. McCubbin, et al., Volatiles (H, C, N, F, S, Cl) in the lunar mantle, crust, and regolith: distribution, processes, sources, and significance, Am. Mineral. 100 (2015) 1668–1707.
[51] G. Heiken, D.S. McKay, *Petrology of a Sequence of Pyroclastic Rocks from the Taurus-Littrow (Apollo 17 Landing Site)* (No. LA-UR-78-1358; CONF-780314-5), Los Alamos National Laboratory (LANL), Los Alamos, NM (United States), 1978.
[52] P. Gay, M.G. Bown, I.D. Muir, Mineralogical and petrographic features of two Apollo 14 rocks, in: Proceedings of the Lunar Science Conference, vol. 3, 1972, p. 351.
[53] J.W. Delano, Pristine lunar glasses: Criteria, data, and implications, J. Geophys. Res. Solid Earth 91 (1986) D201–D213.
[54] A.E. Bence, J.J. Papike, Pyroxenes as recorders of lunar basalt petrogenesis: chemical trends due to crystal-liquid interaction, in: Proc. 3rd Lunar Sci. Conf., vol. 1, 1972, pp. 431–469.
[55] C.C. Allen, R.V. Morris, D.S. McKay, Oxygen extraction from lunar soils and pyroclastic glass, J. Geophys. Res. Planets 101 (1996) 26085–26095.
[56] J. Arndt, W.V. Engelhardt, I. Gonzalez-Cabeza, B. Meier, Formation of Apollo 15 green glass beads, J. Geophys. Res. Solid Earth 89 (1984) C225–C232.
[57] H. Hui, et al., Cooling rates of lunar orange glass beads, Earth Planet Sci. Lett. 503 (2018) 88–94.
[58] X. Zeng, et al., Micro-FTIR spectroscopy of lunar pyroclastic and impact glasses as a new diagnostic tool to discern them, J. Geophys. Res. Planets 124 (2019) 3267–3282.
[59] M.T. Naney, D.M. Crowl, J.J. Papike, The Apollo 16 drill core—Statistical analysis of glass chemistry and the characterization of a high alumina-silica poor (HASP) glass, in: Proc. 7th Lunar Planet. Sci. Conf., Pergamon, 1976, pp. 155–184.
[60] R.L. Korotev, The great lunar hot spot and the composition and origin of the Apollo mafic ("LKFM") impact-melt breccias, J. Geophys. Res. Planets 105 (2000) 4317–4345.
[61] E.C.T. Chao, J.A. Boreman, J.A. Minkin, O.B. James, G.A. Desborough, Lunar glasses of impact origin: physical and chemical characteristics and geologic implications, J. Geophys. Res. 75 (1970) 7445–7479.
[62] L.P. Keller, D.S. McKay, The nature and origin of rims on lunar soil grains, Geochem. Cosmochim. Acta 61 (1997) 2331–2341.
[63] R.N. Clark, Chapter 1: spectroscopy of rocks and minerals, and principles of spectroscopy, in: A.N. Rencz (Ed.), Manual of Remote Sensing, Volume 3, Remote Sensing for the Earth Sciences, John Wiley and Sons, New York, 1999, pp. 3–58.
[64] E.A. Cloutis, M.J. Gaffey, Pyroxene spectroscopy revisited: spectral-compositional correlations and relationship to geothermometry, J. Geophys. Res. Planets 96 (1991) 22809–22826.
[65] G. Zanotti, I. Troisi, A. Dottori, M.R. Lavagna, Planetary soil simulant characterisation: NU-LHT-2M study case to support oxygen extraction lab tests with a low-temperature carbothermal process, Aerospace 11 (2024) 295.
[66] J.M. Long-Fox, et al., Geomechanical properties of lunar regolith simulants LHS-1 and LMS-1, Adv. Space Res. 71 (2023) 5400–5412.
[67] K. Righter, Volatile element depletion of the Moon—The roles of precursors, post-impact disk dynamics, and core formation, Sci. Adv. 5 (2019), https://doi.org/10.1126/sciadv.aau7658 eaau7658.
[68] R. Montelli, G. Nolet, F.A. Dahlen, G. Masters, E.R. Engdahl, S.H. Hung, Finite-frequency tomography reveals a variety of plumes in the mantle, Science 303 (5656) (2004) 338–343.
[69] R.V. Morris, The surface exposure (maturity) of lunar soils: some concepts and Is/FeO compilation, Proc. 9th Lunar Sci. Conf. (1978) 2287–2297.
[70] D.S. McKay, et al., Apollo 14 soils: size distribution and particle types, Proc. 3rd Lunar Sci. Conf. (1972) 983–995.
[71] W. von Engelhardt, J. Arndt, D. Stöffler, H. Schneider, Apollo 14 regolith and fragmental rocks, their compositions and origins by impacts, Proc. 3rd Lunar Sci. Conf. vols. 753–770 (1972).
[72] C.B. Moore, et al., Total carbon, nitrogen and sulfur in Apollo 14 lunar samples, Proc. 3rd Lunar Sci. Conf. vols. 2051–2058 (1972).
[73] J.B. Adams, Visible and near-infrared diffuse reflectance spectra of pyroxenes as applied to remote sensing of solid objects in the solar system, J. Geophys. Res. 79 (1974) 4829–4836.
[74] R.G. Burns, Spectral mineralogy of terrestrial planets: scanning their surfaces remotely, Mineral. Mag. 53 (1989) 135–151.
[75] C.M. Pieters, Strength of mineral absorption features in the transmitted component of near-infrared reflected light: first results from RELAB, J. Geophys. Res. Solid Earth 88 (B11) (1983) 9534–9544.
[76] D.B. Nash, J.E. Conel, Spectral reflectance systematics for mixtures of powdered hypersthene, labradorite, and ilmenite, J. Geophys. Res. 79 (11) (1974) 1615–1621.
[77] B.H. Horgan, E.A. Cloutis, P. Mann, J.F. Bell, Near-infrared spectra of ferrous mineral mixtures and methods for their identification in planetary surface spectra, Icarus 234 (2014) 132–154.
[78] D.P. Moriarty, C.M. Pieters, Complexities in pyroxene compositions derived from absorption band centers: examples from Apollo samples, HED meteorites, synthetic pure pyroxenes, and remote sensing data, Meteorit. Planet. Sci. 51 (2016) 207–234.
[79] C.N. Yasanayake, et al., The spectral characteristics of lunar agglutinates: Visible–near-infrared spectroscopy of apollo soil separates, J. Geophys. Res. Planets 129 (2024) e2023JE008115.
[80] J.L. Provis, J.S.J. van Deventer, Alkali Activated Materials: State-Of-The-Art Report. RILEM TC 224-AAM, Springer, 2014.
[81] A. Palomo, et al., Chemical stability of cementitious materials based on metakaolin, Cement Concr. Res. 29 (1999) 997–1004.
[82] I. García-Lodeiro, A. Palomo, A. Fernández-Jiménez, D.E. Macphee, Compatibility studies between N-A-S-H and C-A-S-H gels. Study in the ternary diagram Na_2O–CaO–Al_2O_3–SiO_2–H_2O, Cement Concr. Res. 41 (2011) 923–931.
[83] B. Walkley, et al., Phase evolution of C-(N)-A-S-H/N-A-S-H gel blends investigated via alkali-activation of synthetic calcium aluminosilicate precursors, Cement Concr. Res. 89 (2016) 120–135.
[84] S. Pilehvar, et al., Utilization of urea as an accessible superplasticizer on the moon for lunar geopolymer mixtures, J. Clean. Prod. 247 (2020) 119177.
[85] H.A. Toutanji, S. Evans, R.N. Grugel, Performance of lunar sulfur concrete in lunar environments, Constr. Build. Mater. 29 (2012) 444–448.
[86] D. Stoeser, D. Rickman, S. Wilson, Design and Specifications for the Highland Regolith Prototype Simulants NU-LHT-1M and-2M, 2011 (No. NASA/TM-2010-216438).
[87] Collins, et al., Mechanical behavior of lunar regolith simulant-based geopolymer under simulated lunar surface temperature, Acta Astronaut. 180 (2021) 211–220.
[88] X. Zheng, C. Zhao, X. Sun, W. Dong, Lunar regolith geopolymer concrete for in-situ construction of lunar bases: a review, Polymers 16 (11) (2024) 1582.
[89] J. Gu, Q. Ma, Experimental study on geopolymerization of lunar soil simulant under dry curing and sealed curing, Materials 17 (6) (2024) 1413.
[90] M. Shaw, The carbothermal reduction of lunar regolith under high-vacuum conditions, Vacuum 233 (2025) 114039.
[91] L. Schlüter, A. Cowley, Review of techniques for In-Situ oxygen extraction on the moon, Planet. Space Sci. 181 (2020) 104753.